

Magnetic Field Amplification via Protostellar Disc Dynamos

S. Dyda,¹ R.V.E. Lovelace,² G.V. Ustyugova,³ A.V. Koldoba⁴ & I. Wasserman^{1,2}

¹*Department of Physics, Cornell University, Ithaca, NY 14853:email: sd449@cornell.edu*

²*Department of Astronomy, Cornell University, Ithaca, NY 14853*

³*Keldysh Institute for Applied Mathematics, Moscow, Russia*

⁴*Moscow Institute of Physics & Technology, Dolgoprudny, Moscow Region 141700, Russia*

3 August 2015

ABSTRACT

We model the generation of a magnetic field in a protostellar disc using an α -dynamo and perform axisymmetric magnetohydrodynamics (MHD) simulations of a T Tauri star. We find that for small values of the dimensionless dynamo parameter α_d the poloidal field grows exponentially at a rate $\sigma \propto \Omega_K \sqrt{\alpha_d}$, before saturating to a value $\propto \sqrt{\alpha_d}$. The dynamo excites dipole and octupole modes, but quadrupole modes are suppressed, because of the symmetries of the seed field. Initial seed fields too weak to launch MHD outflows are found to grow sufficiently to launch winds with observationally relevant mass fluxes of order $10^{-9} M_{\odot}/\text{yr}$ for T Tauri stars. For large values of α_d magnetic loops are generated over the entire disc. These quickly come to dominate the disc dynamics and cause the disc to break up due to the magnetic pressure.

Key words: accretion, accretion discs - dynamo - MHD - stars: magnetic fields - stars: protostars - stars: winds, outflows

1 INTRODUCTION

Magnetic fields play a key role in transporting angular momentum away from protostellar systems, thereby allowing matter to accrete on time scales consistent with models of protostellar evolution. Turbulent viscosity in the accretion disc, most likely generated by the magnetorotational instability (MRI), plays a key role in setting the accretion rate in the disc (Balbus & Hawley 1991). Astrophysical jets and winds are the dominant mechanisms for transporting angular momentum away from protostellar systems. Magnetic fields play a central role in the launching and collimation of these outflows. The origin of these large-scale, ordered, magnetic fields required for sustaining jets and winds is at present not well understood.

One possibility is that the magnetic field is advected inwards from the interstellar medium or ambipolar diffusion (see Shu, Adams & Lizano 1987 for review). Another possibility is that the field is generated locally via a dynamo mechanism. It is interesting therefore, to simulate the effects of a magnetic disc dynamo on protostellar evolution.

Different theoretical dynamo models have been proposed. The mean field dynamo (Moffatt, 1978) relies on a magnetic field that is disordered on small scales interacting through the mean motion of the disc on large scales. Tout &

Pringle's (1992) mechanism relied on the Parker instability, MRI and magnetic reconnections.

Observations suggest that a dynamo mechanism is responsible, at least in part, for the magnetic fields near protoplanetary stars. Empirical evidence suggests there is a correlation between the magnitude of large scale magnetic fields and seed fields, suggesting a related dynamo mechanism is responsible for generating them (Vidotto et al, 2014). Rotational modulation of Zeeman signature in GQ Lup (Donati et al. 2012) and DN Tau (Donati et al. 2013) suggests that the magnetic fields of T Tauri stars are generated by non-stationary dynamos.

Much work has been done to understand the dynamo process in the context of generating turbulent magnetic fields to model the MRI. Stratified shearing box simulations with zero net vertical magnetic flux exhibit a flipping of the mean toroidal magnetic field flux on time scales of roughly 10 orbits (Brandenburg et al. 1995; Shi et al. 2010; Davis et al. 2010, Simon et al. 2012). This effect is found to be more sporadic as the amount of net vertical magnetic flux is increased (Bai & Stone 2013). Full 3D simulations (Stone et al. 1996) of turbulent field evolution largely agreed with these shearing box models. Del Zanna et al. (2014) implemented a disc dynamo in the GRMHD code ECHO and

found exponential growth of toroidal magnetic fields from a seed poloidal field. Sadowski et al. (2014) used a sub-grid model in the GRMHD code KORAL to simulate a dynamo in a thick disc in 2D and found accretion rates were comparable to 3D simulations. The disc dynamo played a key role, by allowing for the regeneration of poloidal magnetic field which drove the disc to a state characteristic for a 3D MRI disc. Schober et al (2012) have shown that dynamo mechanisms can amplify magnetic fields during the formation of primordial halos by converting kinetic energy from turbulence into magnetic energy. von Rekowski (2003) found that an α^2 dynamo can launch outflows even without an external field. Bardou et al. (2001) simulated the back-reaction of outflows on the disc dynamo and found a vertical velocity can enhance the action of the dynamo. In a series of papers Torkelsson & Brandenburg (1994a;1994b;1994c) studied the parity of generated fields and growth rates of dipolar and quadrupolar magnetic fields from linear and non-linear α -dynamo effects. They found their growth to be chaotic for large enough dynamo number. Stepanovs, Fednt & Sheikhnezami (2014) generated episodic outflows with a time dependent mean field disc dynamo.

In this paper we perform axisymmetric MHD simulations of an α -dynamo operating inside a protostellar accretion disc. We provide an initial weak poloidal seed magnetic field and track its growth and the corresponding MHD outflows. Our goal is to understand how the disc dynamo affects the corresponding outflows and the late time magnetic field structure. The structure of this paper is as follows. In Section 2 we review the disc dynamo contribution to the equations of motion and describe our MHD code. In section 3 we present results, describing how outflows and magnetic field structure around the star are affected by the initial seed field, the dynamo parameter α_d , the disc viscosity α_ν and the magnetic diffusivity α_η . We conclude in Section 4 and discuss implications for future work and observational prospects for classical T Tauri stars (CTTS).

2 DYNAMO MODEL

2.1 Basic Equations

The plasma flows are assumed to be described by the equations of non-relativistic magnetohydrodynamics (MHD). In a non-rotating reference frame the equations are

$$\frac{\partial \rho}{\partial t} + \nabla \cdot (\rho \mathbf{v}) = 0, \quad (1a)$$

$$\frac{\partial \rho \mathbf{v}}{\partial t} + \nabla \cdot \mathcal{T} = \rho \mathbf{g}, \quad (1b)$$

$$\frac{\partial \mathbf{B}}{\partial t} - \nabla \times (\mathbf{v} \times \mathbf{B}) + \nabla \times (\eta_t \nabla \times \mathbf{B}) + \nabla \times (A \mathbf{B}) = 0, \quad (1c)$$

$$\frac{\partial (\rho S)}{\partial t} + \nabla \cdot (\rho \mathbf{v} S) = \mathcal{Q}, \quad (1d)$$

where ρ is the mass density, S is the specific entropy, \mathbf{v} is the flow velocity, \mathbf{B} is the magnetic field, \mathcal{T} is the momentum flux density tensor, $\mathbf{E} = -\mathbf{v} \times \mathbf{B}/c + \eta_t \nabla \times \mathbf{B}/c$ is the electric field, \mathcal{Q} is the rate of change of entropy per unit volume due

to heating, η_t is the turbulent magnetic diffusivity and c is the speed of light.

The dynamo effect is generated by the turbulent fluctuations of the velocity $\delta \mathbf{v}$. Above

$$A = -\frac{\tau}{3} \langle \delta \mathbf{v} \cdot \nabla \times \delta \mathbf{v} \rangle = Z \Omega_K \alpha_d, \quad (2)$$

is the product of the decorrelation time of the velocity fluctuations τ and the mean helicity of the turbulence. We parametrize this by an α prescription, with the strength of the effect parametrized by the α -dynamo parameter α_d . See Kulsrud (1999) for review of the mean field theory dynamo. α_d is a dimensionless number that we vary in our simulations and the prefactor of the height in the disc Z times the local Keplerian angular velocity Ω_K was chosen by dimensional analysis.

We assume that the heating is offset by radiative cooling so that $\mathcal{Q} = 0$. Also, $\mathbf{g} = -(GM/r^2) \hat{r}$ is the gravitational acceleration due to the central mass M . We model the fluid as a non-relativistic ideal gas with equation of state

$$S = \ln \left(\frac{p}{\rho^\gamma} \right), \quad (3)$$

where p is the pressure and $\gamma = 5/3$.

We use cylindrical coordinates (R, ϕ, Z) as these are the coordinates used by our code. Sometimes it will be useful to also refer to spherical coordinates (r, θ, ϕ) as well.

We consider that both the viscosity and the magnetic diffusivity of the disc plasma are due to turbulent fluctuations of the velocity and magnetic field. We assume that the molecular transport coefficients can be replaced by the turbulent coefficients. The turbulent coefficients are parameterized using the α -model of Shakura and Sunyaev (1973). The turbulent kinematic viscosity is

$$\nu_t = \alpha_\nu \frac{c_s^2}{\Omega_K}, \quad (4)$$

where c_s is the midplane sound speed and $\alpha_\nu \leq 1$ is a dimensionless constant. Similarly, the turbulent magnetic diffusivity is

$$\eta_t = \alpha_\eta \frac{c_s^2}{\Omega_K}, \quad (5)$$

where α_η is another dimensionless constant. The ratio,

$$\mathcal{P} = \frac{\alpha_\nu}{\alpha_\eta}, \quad (6)$$

is the magnetic Prandtl number of the turbulence in the disc. Shearing box simulations of MRI driven MHD turbulence in discs indicate that $\mathcal{P} \sim 1$ (Guan & Gammie 2009). We take $\alpha_\nu = \alpha_\eta = 0.1$ unless otherwise stated.

We define the dynamo number

$$N_d = \frac{A \Omega_K h^3}{\eta_t^2} \approx \frac{\alpha_d}{\alpha_\eta^2}. \quad (7)$$

Dynamo effects are thought to be important for $N_d > N_c$ for some critical dynamo number (Stepinski & Levy 1988).

The momentum flux density tensor is given by

$$\mathcal{T}_{ik} = p \delta_{ik} + \rho v_i v_k + \left(\frac{\mathbf{B}^2}{8\pi} \delta_{ik} - \frac{B_i B_k}{4\pi} \right) + \tau_{ik}, \quad (8)$$

where τ_{ik} is the viscous stress contribution from the turbulent fluctuations of the velocity. As mentioned, we assume

that these can be represented in the same way as the collisional viscosity by substitution of the turbulent viscosity. The leading order contributions to the viscous stress arise from large velocity gradients. In a Keplerian type disc these are dominated by the azimuthal terms $v_\phi \sim v_K$. However, we include all viscous terms involving v_R and v_ϕ . The leading order contribution to the momentum flux density from turbulence are therefore

$$\begin{aligned}\tau_{R\phi} &= -\nu_t \rho R \frac{\partial \Omega}{\partial R}, & \tau_{Z\phi} &= -\nu_t \rho R \frac{\partial \Omega}{\partial Z}, \\ \tau_{ZR} &= -\nu_t \rho \frac{\partial v_R}{\partial Z}, & \tau_{RR} &= -2\nu_t \rho \frac{\partial v_R}{\partial R}, \\ \tau_{\phi\phi} &= -2\nu_t \rho \frac{v_R}{R},\end{aligned}\quad (9)$$

where $\Omega = v_\phi/R$ is the angular velocity of the gas.

The transition from the viscous disc to the non-viscous corona is handled by multiplying the viscosity by a dimensionless factor $\xi(\rho)$ which varies smoothly from $\xi = 1$ for $\rho \geq \rho_d = 0.75\rho(R, Z = 0)$ to $\xi = 0$ for $\rho \leq 0.25\rho_d$ as described in Appendix B of Lii, Romanova, & Lovelace (2012).

2.2 Disc Averaged Equations

To gain some insight into the dynamo process, consider a thin, axisymmetric, Keplerian disc with diffusivity η and radial infall velocity v_R operating an α -dynamo. We will ignore any vertical motion v_Z and neglect the Z dependence of Ω and v_R . Breaking the induction equation (1c) into (R, ϕ, Z) components, we find

$$\begin{aligned}-\frac{1}{R} \frac{\partial}{\partial Z} \left(\frac{\partial \Psi}{\partial t} \right) &= \frac{\partial}{\partial Z} \left[-AB_\phi + \frac{v_R}{R} \frac{\partial \Psi}{\partial R} \right. \\ &\quad \left. - \frac{\eta}{R} \left(R \frac{\partial}{\partial R} \left(\frac{1}{R} \frac{\partial \Psi}{\partial R} \right) + \frac{\partial^2 \Psi}{\partial Z^2} \right) \right],\end{aligned}\quad (10a)$$

$$\begin{aligned}\frac{\partial B_\phi}{\partial t} &= -\frac{\partial \Omega}{\partial R} \frac{\partial \Psi}{\partial Z} + \frac{\partial}{\partial Z} \left(-\frac{A}{R} \frac{\partial \Psi}{\partial Z} + \eta \frac{\partial B_\phi}{\partial Z} \right) \\ &\quad - \frac{\partial}{\partial R} \left(\frac{A}{R} \frac{\partial \Psi}{\partial R} + v_R B_\phi - \frac{\eta}{R} \frac{\partial (RB_\phi)}{\partial R} \right),\end{aligned}\quad (10b)$$

$$\begin{aligned}\frac{\partial}{\partial R} \left(\frac{\partial \Psi}{\partial t} \right) &= \frac{\partial}{\partial R} \left[AB_\phi R - v_R \frac{\partial \Psi}{\partial R} \right. \\ &\quad \left. + \eta \left(R \frac{\partial}{\partial R} \left(\frac{1}{R} \frac{\partial \Psi}{\partial R} \right) + \frac{\partial^2 \Psi}{\partial Z^2} \right) \right],\end{aligned}\quad (10c)$$

where Ψ is the magnetic flux function. Two types of solutions are possible, depending on the symmetries of Ψ and B_ϕ - a “dipole” like solution where $\Psi(Z) = \Psi(-Z)$ and $B_\phi(Z) = -B_\phi(-Z)$ and a “quadrupole” solution where $\Psi(Z) = -\Psi(-Z)$ and $B_\phi(Z) = B_\phi(-Z)$ (see Kulsrud 2005). To solve the problem exactly we make a gauge choice, for example $\Psi(0) = 0$ and boundary conditions at $Z = \pm h$ such as $\partial \Psi / \partial Z = 0$. Intuitively then, one may think of the flux function as a cosine in the dipole like case and as a sine in the quadrupole case

$$\Psi(Z) = \begin{cases} \Psi_0 \cos\left(\frac{\pi Z}{h}\right) & \text{“dipole”,} \\ \Psi_0 \sin\left(\frac{\pi Z}{h}\right) & \text{“quadrupole”.} \end{cases}\quad (11)$$

We work in the thin disc, $h \ll R$, approximation. The variation in the flux function over the half disc thickness is therefore in each case $\Delta \Psi \approx \Psi_0$ but the variation in its derivative for each case is $\Delta \Psi / \Delta Z_{\text{dip}} \approx 2\Delta \Psi / \Delta Z_{\text{quad}}$. Therefore integrating over the upper half part of the disc, and replacing all quantities with their vertically averaged quantities $\int_0^h B_\phi dz = h \bar{B}_\phi$, $\int_0^h -\frac{1}{R} \frac{\partial \Psi}{\partial Z} dz = h \bar{B}_R$ and ignoring terms involving B_Z , the R and ϕ components give us the coupled system

$$\frac{\partial \bar{B}_\phi}{\partial t} = \left(\frac{3}{2} C_1 + C_2 \alpha_d \right) \Omega \bar{B}_R - \frac{\eta}{h^2} \bar{B}_\phi, \quad (12a)$$

$$\frac{\partial \bar{B}_R}{\partial t} = C_2 \alpha_d \Omega \bar{B}_\phi - \frac{\eta}{h^2} \bar{B}_R. \quad (12b)$$

where $C_1 = 1(-1)$ and $C_2 = 2(-1)$ in the dipole (quadrupole) case. Using $\eta = \alpha_\eta \Omega h^2$, we combine (12) and find

$$\begin{aligned}\frac{\partial^2 \bar{B}_R}{\partial t^2} + 2\alpha_\eta \Omega \frac{\partial \bar{B}_R}{\partial t} \\ + [\alpha_\eta^2 - C_2 \alpha_d (3/2C_1 + C_2 \alpha_d) +] \Omega^2 \bar{B}_R = 0.\end{aligned}\quad (13)$$

Taking $\bar{B}_R \propto \exp(\sigma \Omega t)$ we find growth rates

$$\sigma = -\alpha_\eta \pm \sqrt{C_2 \alpha_d (3/2C_1 + C_2 \alpha_d)}. \quad (14)$$

Taking $\alpha_d \ll 1$ we approximate

$$\sigma + \alpha_\eta \approx \begin{cases} \pm \sqrt{3\alpha_d} & \text{“dipole”,} \\ \pm \sqrt{3\alpha_d/2} & \text{“quadrupole”.} \end{cases}\quad (15)$$

Substituting back into (12) we find

$$\bar{B}_R \approx \begin{cases} \pm \sqrt{\frac{2\alpha_d}{3}} \bar{B}_\phi & \text{“dipole”,} \\ \mp \sqrt{\frac{2\alpha_d}{3}} \bar{B}_\phi & \text{“quadrupole”.} \end{cases}\quad (16)$$

The toroidal field component is primarily generated by the differential rotation of the disc. It is also the dominant contribution to the magnetic field. Therefore, at late times when the matter and magnetic pressure in the disc are in equilibrium, we expect the toroidal component to saturate. This would imply that the radial field should also saturate, to a value proportional to $\sqrt{\alpha_d}$. For this reason, we scale all our magnetic field plots to $\sqrt{\alpha_d}$. Also, for $\alpha_d, \alpha_\eta \ll 1$ the growth rate $\sigma \propto \sqrt{\alpha_d}$ and we scale all times by a factor of $\alpha_d^{-1/2}$. We note that requiring a positive growth rate $\sigma > 0$ implies $N_d \gtrsim 1/3$. Though we have neglected order one numbers, this provides an intuitive picture for why there is a critical dynamo number - if the diffusion time scale is too fast compared to the dynamo time scale then the field will diffuse away and never grow. Stepinski & Levi (1988) found purely growing dynamo modes for dynamo number $R_m = (R/h)^{3/2} \alpha_d / \alpha_\eta^2 \sim 100$ which agrees with this result up to some $\mathcal{O}(1)$ numbers.

Above we neglected terms that depended on $\partial/\partial R$ to make the exponential growth of the field via the dynamo apparent. However, these terms are important for determining the effects of viscosity and diffusivity in the disc. In particular, taking $v_R = \nu/R$ and ν, η constant and expanding (10) will yield advection like terms $\propto (-\nu + \eta) \partial \Psi / \partial R$ and $(-\nu - \eta) \partial B_\phi / \partial R$. η and ν may cooperate or compete in transporting different field components. We show this empirically in our simulations where the effects of the dynamo can be changed by varying the Prandtl number $\mathcal{P} = \alpha_\nu / \alpha_\eta$.

2.3 Initial Conditions

2.3.1 Magnetic Field & Dynamo

Our simulations use a disc field (Zanni, 2007) as a seed field for the dynamo, defined by the poloidal flux function

$$\Psi_{\text{disc}} = \frac{4}{3} B_0 R_0^2 \left(\frac{R}{R_0} \right)^{3/4} \frac{m^{5/4}}{(m^2 + Z^2/R^2)^{5/8}}, \quad (17)$$

where the poloidal magnetic field components can be computed via

$$B_Z = \frac{1}{R} \frac{\partial \Psi}{\partial R}, \quad B_R = -\frac{1}{R} \frac{\partial \Psi}{\partial Z}. \quad (18)$$

The parameter m determines how much the field lines bend in the R - Z plane with the limit $m \rightarrow \infty$ corresponding to purely vertical field lines. In this study we set $m = 1$.

The field generated by the dynamo can be expanded using a multipole expansion

$$\Psi = \mu_{\text{dip}} \Psi_{\text{dip}} + \mu_{\text{quad}} \Psi_{\text{quad}} + \mu_{\text{oct}} \Psi_{\text{oct}} + \dots \quad (19)$$

where

$$\Psi_{\text{dip}} = \frac{R^2}{(R^2 + Z^2)^{3/2}}, \quad (20)$$

is the dipole contribution to the potential,

$$\Psi_{\text{quad}} = \frac{3}{4} \frac{R^2 Z}{(R^2 + Z^2)^{5/2}}, \quad (21)$$

is the quadrupole contribution and

$$\Psi_{\text{oct}} = \frac{R^2 (4Z^2 - R^2)}{2(R^2 + Z^2)^{7/2}}, \quad (22)$$

is the octupole contribution. These are expected to be the dominant modes excited by the disc dynamo. The disc dynamo is given by

$$A(R, Z) = \begin{cases} 0 & R < R_{\text{dyn}}, \\ \alpha_d Z \sqrt{\frac{GM}{R^3}} e^{-(\rho_{\text{dyn}}/\rho)^2} \tanh\left(\frac{R - R_{\text{dyn}}}{\Delta R}\right) & R > R_{\text{dyn}}. \end{cases} \quad (23)$$

In our simulations we have set $R_{\text{dyn}} = 5$, $\rho_{\text{dyn}} = 0.1$ and $\Delta R = 1$. This is the form of the α -dynamo described in (2) but with an exponential factor to continuously cut it off from operating in the corona and a hyperbolic tangent to continuously cut it off at an inner radius R_{dyn} . We found it necessary to impose an inner disc cutoff to avoid numerical instabilities at the surface of the star.

2.3.2 Matter Distribution

Initially the matter of the disc and corona are assumed to be in mechanical equilibrium (Romanova et al. 2002). The initial density distribution is taken to be barotropic with

$$\rho(p) = \begin{cases} p/T_{\text{disc}} & p > p_b \text{ and } R \geq R_d, \\ p/T_{\text{cor}} & p < p_b \text{ or } R \leq R_d, \end{cases} \quad (24)$$

where p_b is the level surface of pressure that separates the cold matter of the disc from the hot matter of the corona and R_d is the initial inner disc radius. At this surface the density has an initial step discontinuity from value p/T_{disc} to p/T_{cor} .

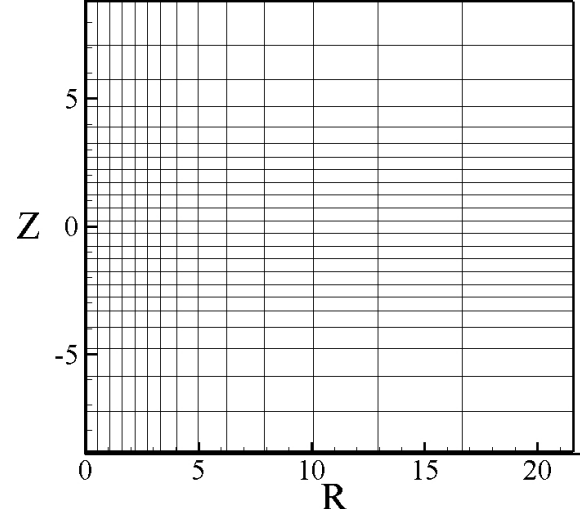


Figure 1. Sparse version of grid used in the simulations, showing every 11th gridline in the R direction and every 10th gridline in the Z direction.

Because the density distribution is barotropic, the initial angular velocity is a constant on coaxial cylindrical surfaces about the Z -axis. Consequently, the pressure can be determined from the Bernoulli equation

$$F(p) + \Phi + \Phi_c = B_0, \quad (25)$$

here B_0 is Bernoulli's constant, $\Phi = -GM/\sqrt{R^2 + Z^2}$ is the gravitational potential, with $GM = 1$ in the code, $\Phi_c = \int_R^\infty r dr \omega^2(r)$ is the centrifugal potential, and

$$F(p) = \begin{cases} T_{\text{disc}} \ln(p/p_b) & p > p_b \text{ and } R \geq R_d, \\ T_{\text{cor}} \ln(p/p_b) & p < p_b \text{ or } R \leq R_d. \end{cases} \quad (26)$$

We take the Bernoulli parameter $B_0 = 3 \times 10^{-4}$ in our simulations. The initial half thickness of the disc $h/R = 0.1$ at the initial inner disc edge $R_d = 5$.

2.3.3 Angular Velocity

The initial angular velocity of the disc is slightly sub-Keplerian,

$$\Omega = (1 - 0.003)\Omega_K(R) \quad R > R_d, \quad (27)$$

Inside of R_d , the matter rotates rigidly with angular velocity

$$\Omega = (1 - 0.003)\Omega_K(R_d) \quad R \leq R_d. \quad (28)$$

The corotation radius R_c is the radius where the angular velocity of the disc equals that of the star; that is, $R_c = (GM/\Omega_*^2)^{1/3}$. In this study we have chosen $R_c = 2$.

2.4 Boundary Conditions

Our simulation region has three boundaries: the axis, the surface of the star and the external boundaries. For each dynamical variable we impose a boundary condition consistent with our physical assumptions.

Parameters	Symbol	Value
mass	M_0	1.59×10^{33} g
length	R_0	1.50×10^{12} cm
magnetic field	B_0	8.04×10^{-2} G
time	P_0	3.53×10^{-2} y
velocity	v_0	8.42×10^7 cm/s
density	ρ_0	7.24×10^{-15} g/cm ³
accretion rate	\dot{M}_0	2.72×10^{-7} M_\odot /yr
temperature	T_0	4.26×10^7 K
dipole strength	μ_{dip}	2.69×10^{35} G cm ³
quadrupole strength	μ_{quad}	4.04×10^{47} G cm ⁴
octupole strength	μ_{oct}	6.05×10^{59} Gcm ⁵

Table 1. Mass, length, and magnetic field scales of interest and the corresponding scales of other derived quantities for a CTTS. One can obtain the physical values from the simulation values by multiplying by the corresponding dimensional quantity above.

We assume axisymmetry about the axis. On the star and the external boundaries we want to allow fluxes and impose free boundary conditions $\partial\mathcal{F}/\partial n = 0$ where \mathcal{F} is a dynamical variable and n is the vector normal to the boundary.

At the external boundary along the edge of the disc we allow new matter to flow into the simulation region. We impose the condition that the matter must be accreting $v_r < 0$. In the coronal region, we prescribe outflow conditions and allow matter, entropy and magnetic flux to exit the simulation region.

The star is taken to be cylindrical in shape with radius $R_* = 1$ and height $Z_* = 2$. Free boundary conditions are imposed on the variables ρ , p and \mathbf{B} . In addition, we require that matter on the stellar boundary flow into the star. We treat the corner of the star by averaging over the nearest neighbour cells in the R and Z directions.

Our simulation uses a grid $N_R \times N_Z = 154 \times 230$ cells. The star has a radius of 1 in units of the simulation and is cylindrical in shape. It extends 10 grid cells above and below the equatorial plane. In the R-direction, the first 60 grid cells have length $dR = 0.05$. Later cell lengths are given recursively by $dR_{i+1} = 1.025dR_i$. Similarly, in the Z-direction the first 30 grid cells above and below the equatorial plane have length $dZ = 0.05$. Later cell lengths are given recursively by $dZ_{j+1} = 1.025dZ_j$. We show a sparse version of our grid, showing every 11th gridline in the R direction and every 10th gridline in the Z direction in Fig. 1.

2.5 Dimensional Variables

The MHD equations are written in dimensionless form so that the simulation results can be applied to different types of stars. We assume that the central object is a CTTS with mass $M_* = 0.8M_\odot$, a radius $R_* = 2R_\odot$ and a magnetic field with magnitude $B_* = 3 \times 10^3$ G on the stellar surface, which is typical for the magnitude of the stellar dipole. We define dimensionful quantities with a 0 subscript, to denote typical values of physical parameters at a reference radius R_0 . The mass scale is set by the stellar mass so $M_0 = M_*$. The reference length, $R_0 = 0.1$ AU, is taken to be the scale

of a typical inner disc radius. Assuming a stellar dipole field, the magnetic field strength $B_0 = B_*(R_*/R_0)^3$. The mass, length and magnetic field scales allow us to define all other dimensionful quantities.

The reference value for the velocity is the Keplerian velocity at the radius R_0 , $v_0 = (GM_0/R_0)^{1/2}$. The reference time-scale is the period of rotation at R_0 , $P_0 = 2\pi R_0/v_0$. From the relation $\rho_0 v_0^2 = B_0^2/4\pi$, we define the reference density ρ_0 of the disc. This also defines a reference pressure. The reference mass accretion rate is $\dot{M}_0 = 4\pi\rho_0 v_0 R_0^3$. The reference temperature $T_0 = v_0^2/2 \times m_H/k_B$ where m_H is the atomic mass of hydrogen and k_B , the Boltzmann constant, is obtained by taking the ratio of the reference pressure $p_0 = B_0^2/8\pi$ and the reference density. The dimensions of the coefficients in the multipole expansion of the flux function are obtained by scaling the reference field by the appropriate power of R_0 - $\mu_{\text{dip}} = B_0 R_0^3$, $\mu_{\text{quad}} = \mu_{\text{dip}} R_0$ and $\mu_{\text{oct}} = \mu_{\text{dip}} R_0^2$.

Results obtained in dimensionless form can be applied to objects with widely different sizes and masses. However, the present work focuses on CTTS with the typical values shown in Table 1. One can obtain dimensionful quantities from simulation results by multiplying by the appropriate dimensionful quantity above. A more detailed description of our code and numerical methods can be found in Koldoba et al. (2015).

3 RESULTS

The α -dynamo converts a poloidal magnetic field into a toroidal magnetic field and vice versa. We provide an initial poloidal seed field. The differential disc rotation causes a twisting of this poloidal field, producing a toroidal field. The α dynamo in turn converts this toroidal field into poloidal field. This is a positive feedback loop and the poloidal field continues to grow until other physical effects halt the growth. This could have interesting observational implications, as seed fields too weak to launch MHD outflows can grow to values which can support observable outflows.

We find two qualitatively different regimes in our dynamo simulations - a *weak dynamo* regime where dynamo effects are only important in the inner disc and a *strong dynamo* regime where dynamo effects affect the entire disc and the magnetic field quickly comes to dominate the disc dynamics. We discuss our results for each of these cases below.

3.1 Weak Dynamo

Below we show poloidal plots of disc density ρ , magnetic flux contours Ψ and poloidal velocity vectors v_p of a typical run in the weak dynamo regime (Fig. 2). We see that magnetic flux of the disc increases as a function of time, and the flux builds up on the star as it advects inwards with the accreting matter. The dynamo only changes the field geometry in the inner part of the disc $R \lesssim 10$ where loops form, even though the dynamo is operating for all radii $R > R_{\text{dyn}} = 5$. In the outer parts of the disc field lines become more inclined relative to their initial configuration, just like in the case where the dynamo is not operating.

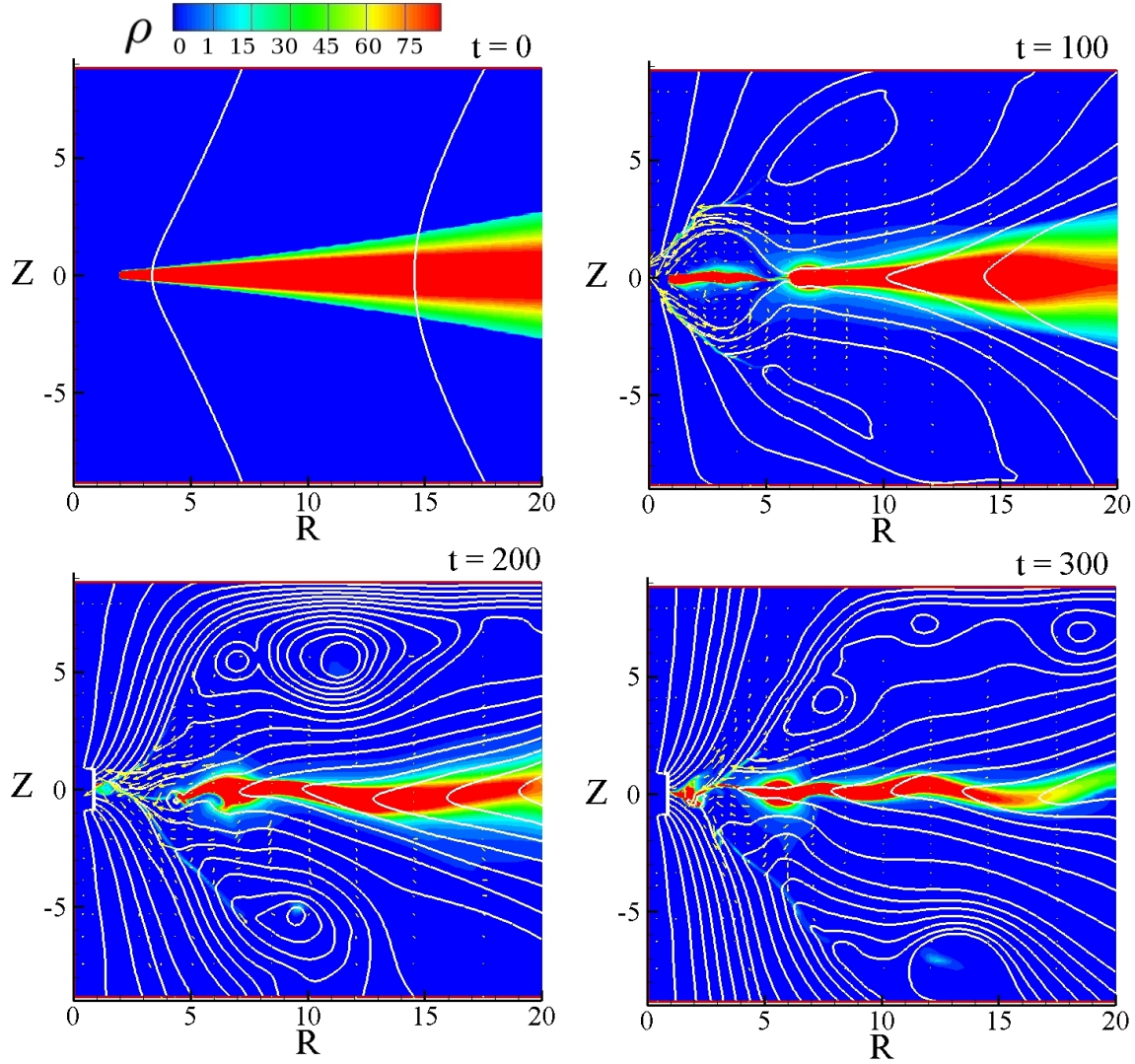


Figure 2. Density ρ (color), poloidal field lines Ψ (white) and poloidal velocity v_p for the case $N_d = 10$. $t = 0$ shows the initial large scale field. By $t = 100$ the dynamo has changed the field structure in the inner part of the disc. By $t = 200$ the field has developed a parallel dipole structure near the star, which interacts with the large scale field to produce an X-point at $R \approx 6$. By $t = 300$ the dipole structure has pushed out the inner part of the disc.

3.1.1 Stellar Multipoles

Any magnetic field can be expanded in a general multipole expansion. As our code is in cylindrical coordinates, projecting out the multipole components is slightly more involved than taking the inner product of the flux function with the Legendre polynomials. We show how to extract the dipole μ_{dip} , quadrupole μ_{quad} and octupole μ_{oct} moments from our simulations in Appendices A1 - A3. We use this method to study the time dependence of the multipole moments. This gives us a sense of the geometry of the generated magnetic field around the star. This is important because measurements using the Zeeman-Doppler technique have shown that magnetic fields around young stars are often complex, exhibiting dipole and higher order fields (e.g. Donati & Collier Cameron 1997; Donati et al. 1999; Jardine et al. 2002).

Runs were performed with seed field amplitudes ranging between $B_0 = 10^{-2} - 10^0$. These correspond to mid-plane plasma $\beta = 10^1 - 10^5$. For $\beta \gg 10^1$, corresponding to seed fields $B_0 \ll 1$, the results were largely independent of the initial magnetic field. For larger field values, the dynamo had comparatively little effect, and the simulation behaved as for the case $\alpha_d = 0$ where the disc dynamo is explicitly turned off. Growth of the dipole and higher order moments around the star is due to advection and rearrangement of the field, and not the generation of new magnetic flux. Cowling's antidydro theorem (1934) states that a self-sustained, axisymmetric field cannot be maintained - in essence non axisymmetric velocity components must counteract the diffusion of the field. Our simulations run on the order of 600 orbits at $R = 1$, corresponding to roughly 6 orbits at $R = 20$. The typical diffusion time $\tau \sim R^2/\eta_t \gg 1$,

meaning we can evade the antidynamo theorem because we have not waited sufficiently long for the field to diffuse away. In fact, after $t = 600$ the total magnetic flux threading the star and disc decreased roughly 5% from its initial value. The flux on the star increased roughly 100% and the flux threading the disc decreased approximately 20%.

For fixed diffusivity $\alpha_\eta = 0.1$ and seed field amplitude $B_0 = 0.1$ we plot the dipole (Fig. 3), quadrupole (Fig. 4) and octupole moments (Fig. 5) as a function of time for dynamo numbers $N_d = 1, 5, 10$ ($\alpha_d = 0.01, 0.05$ and 0.1). We have scaled the time by $\alpha_d^{1/2}$ and the dipole moment by $\alpha_d^{-1/2}$, as suggested by the linear analysis of Section 2.2. Empirically, we see this scaling yields similar behaviour for runs with different dynamo strength parameter when $\alpha_d \ll 1$. We find qualitatively different behaviour of the dipole, quadrupole and octupole moments. The dipole moment grows to a value of approximately $\mu_{\text{dip}} \approx -N_d^{1/2}$. It saturates to this value on time scales $\tau \sim \alpha_d^{-1/2} \Omega_K (R_{\text{dyn}})^{-1}$. The quadrupole moment oscillates about $\mu_{\text{quad}} = 0$, which is what we would expect given the symmetry of the initial seed field. The magnitude of these oscillations increases with increasing dynamo number. At late times the amplitude of the oscillations dies down. The octupole moment begins to oscillate at the same time that the dipole mode begins to grow. In the cases where $\alpha_d = 0.05$ or 0.1 when the dipole reaches its asymptotic value, the octupole moment quickly assumes the opposite sign so that the late time octupole moment saturates at the same time as the dipole but with opposite polarity. This suggests that the lower order multipole moments are excited first, and higher order multipoles will be excited and grow as the lower order poles reach a saturation value. The octupole moment saturates to a value of $\mu_{\text{oct}} \approx -N_d^{1/2}$ as suggested by the linear theory. For weaker dynamos, the higher order modes are not excited. These results are consistent with the symmetries of the seed field - the disc dynamo is a symmetric function of position Z , therefore we expect to excite symmetric (dipole and octupole) and not asymmetric (quadrupole) modes. Reversing the polarity of the seed field reverses the signs of the generated multipoles, but does not otherwise change the results, as expected.

We term this the weak dynamo regime because the physics is largely determined by what is happening in the inner disc. In particular, we performed simulations where we varied the cutoff radius $5 \leq R_{\text{dyn}} \leq 8$ but kept the dynamo coefficient A in (23) constant at R_{dyn} by varying α_d . The late time moments changed by roughly 10% and growth rates and times were similarly affected. Poloidal field plots retained the same qualitative character, where a large loop formed near the cutoff radius but field lines in the outer disc tilted more towards the equatorial plane of the disc.

3.1.2 Growth Rate

The disc averaged equations predict that the exponential growth rate $\sigma \propto \sqrt{\alpha_d} \Omega_K$, scaling like $\sqrt{\alpha_d}$ and the local Keplerian angular velocity. We plot vertically integrated \bar{B}_Z at radii $R = 10, 15$ and 20 as a function of angular phase $\Omega_K t$ for the case $\alpha_d = 0.1$ (Fig. 6). We scale the magnetic field by $\alpha_d^{-1/2}$ and the phase by $\alpha_d^{1/2}$ for ease in comparison of the other simulations. We see that there is indeed a period

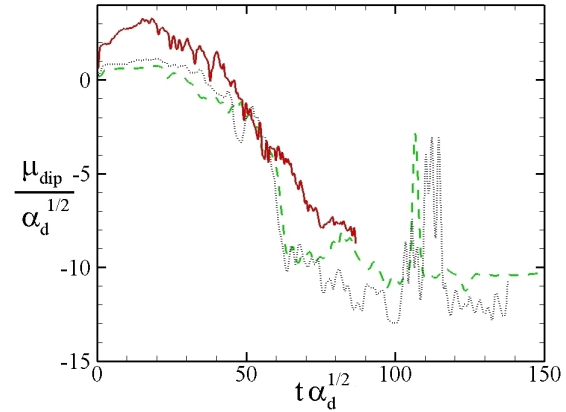


Figure 3. Dipole moment μ_{dip} as a function of time for dynamo numbers $N_d = 1$ (red, solid), 5 (black, dot) and 10 (green, dash). These runs had a constant disc diffusivity $\alpha_\eta = 0.1$ and the dynamo number was varied using the α_{dyn} parameter. By scaling the time axis to $\alpha_d^{1/2}$ and the dipole moment μ_{dip} to $\alpha_d^{-1/2}$ we see the universal scaling of the late time dipole moment and of the growth rate.

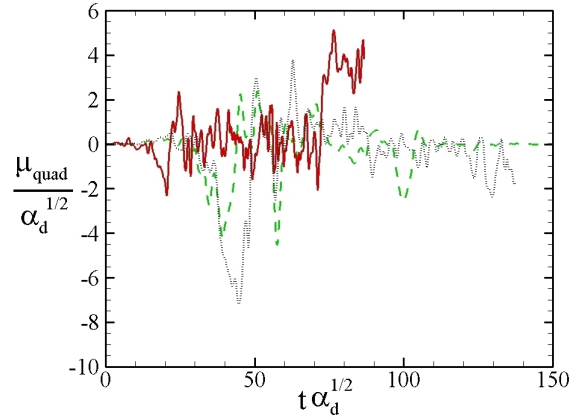


Figure 4. Quadrupole moment μ_{quad} as a function of time for dynamo numbers $N_d = 1$ (red, solid), 5 (black, dot), 10 (green, dash). These runs had a constant disc diffusivity $\alpha_\eta = 0.1$ and the dynamo number was varied using the α_{dyn} parameter. We have scaled the time axis to $\alpha_d^{1/2}$ and the quadrupole moment μ_{quad} to $\alpha_d^{-1/2}$.

of exponential growth lasting a time scale of $\mathcal{O}(1)$ where the field likewise changes by $\mathcal{O}(1)$. The scaling (15) suggests that $\sigma \approx \sqrt{3}$ in these units but we find, averaging the rates for these three radii and $\alpha_d = 0.01, 0.05$ and 0.1 runs $\sigma = 2.0 \pm 1.0$. This suggests that our linear analysis where we dropped order one numbers is valid during this short time. At late times a gap begins to form for $R < R_{\text{dyn}}$, as the inner disc becomes magnetically dominated owing to the advected magnetic flux.

The magnetic field strength in the disc is also found to

increase in time. We define the averaged field in the disc via

$$\bar{B}_i = \left(\frac{\int_{\rho > \rho_{\text{floor}}} (B_i)^2 dV}{\int_{\rho > \rho_{\text{floor}}} dV} \right)^{1/2}, \quad (29)$$

where $\rho_{\text{floor}} = 1$. We define the averaged field in this way because B_R and B_ϕ are antisymmetric about the disc plane and average out to zero vertically. We show a plot of \bar{B}_R/\bar{B}_ϕ and \bar{B}_R as functions of time in Fig. 7 and Fig. 8. We see that the radial magnetic field is an increasing function of time and grows nearly linearly. We see that the ratio of radial to toroidal magnetic field is, to an order one number, constant over the simulation time. This suggests that the simple picture whereby differential rotation creates toroidal field, and the α -dynamo transforms this field into poloidal field

is qualitatively correct. Unlike on the surface of the star, where the field saturates at late times in the simulation, the integrated field in the disc continues to grow. Since the growth rate is set by the local Keplerian time, on time scales of the simulation the outer part of the disc does not have time to saturate with magnetic field, whereas near the star, where time scales are expected to be shorter and field is advected inwards at a faster rate the field has time to saturate. We can estimate the growth rate of \bar{B} by assuming a local exponential growth rate $\sigma t \Omega_K$ and initially uniform field B_0 in which case $\int B_0^2 e^{2\sigma t \sqrt{GM} R^{-3/2}} R dR \sim t^{4/3}$. If the field were decreasing radially then this dependence on t would be weaker. The greatest contribution of this integral occurs for $\sigma \Omega t \gtrsim 1$ so there is a characteristic radius $R_{\text{max}} \propto t^{2/3}$ beyond which there is little contribution. We find $\bar{B} \sim t^{1.1}$ so a

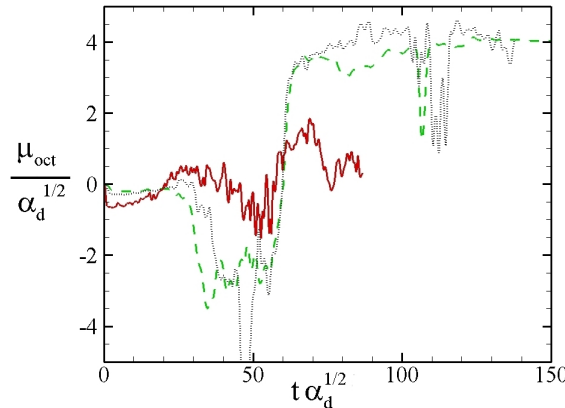


Figure 5. Octupole moment μ_{oct} as a function of time for dynamo numbers $N_d = 1$ (red, solid), 5 (black, dot) and 10 (green, dash). These runs had a constant disc diffusivity $\alpha_\eta = 0.1$ and the dynamo number was varied using the α_d parameter. Note how the octupole component has the opposite sign of the dipole component at late times.

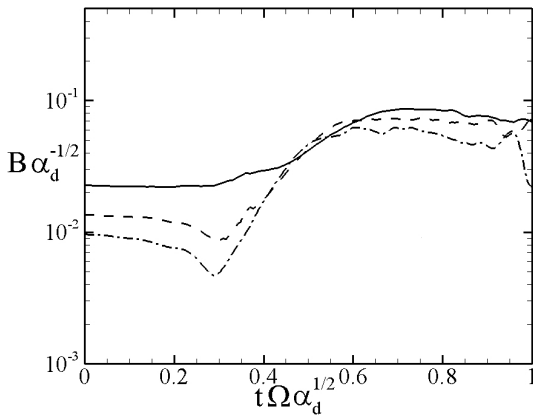


Figure 6. Vertically integrated magnetic field \bar{B}_Z at radii $R = 10$ (solid), 15 (dash) and 20 (dash – dot) as a function of angular phase Ωt scaled by $\alpha_d^{1/2}$ for the case $\alpha_d = 0.1$. The exponential growth predicted by the linearized regime occurs for phase angles $t \Omega \sqrt{\alpha_d} \ll 1$

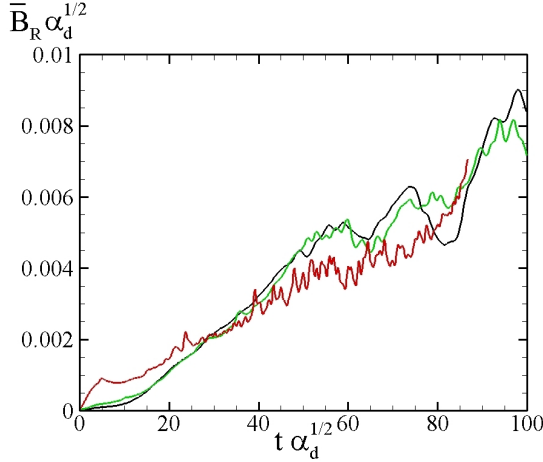


Figure 7. Average radial magnetic field strength \bar{B}_R computed from 29 for the cases $\alpha_d = 0.01$ (red), 0.05 (green) and 0.1 (black). Unlike the field around the star, the disc averaged magnetic field does not have time to saturate on time scales of the simulation.

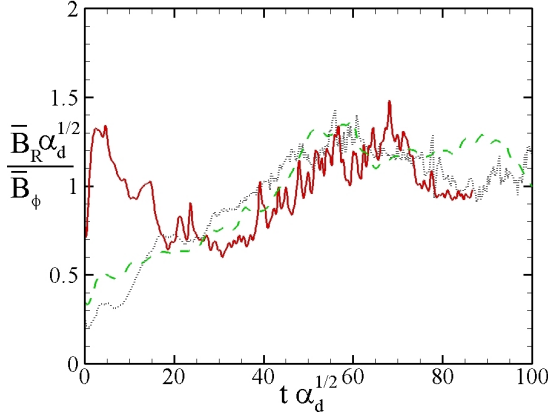


Figure 8. Average radial magnetic field strength \bar{B}_R / \bar{B}_ϕ computed from 29 for the cases $\alpha_d = 0.01$ (red), 0.05 (green) and 0.1 (black). This ratio varies by an order one number, suggesting that the picture where toroidal field is built up via differential rotation and a fraction of this is converted to poloidal field via dynamo action is qualitatively correct.

slightly stronger dependence than predicted by this model. However, it provides a semi-quantitative understanding of how polynomial growth is achieved globally whereas growth is exponential locally.

3.1.3 Outflows

An interesting question is how the field generated by the dynamo affects matter outflows. We measure the total mass flux \dot{M} at the outer boundaries $Z = \pm 5$ for various dynamo numbers (Fig. 9). Choosing to measure mass flux along boundaries in the range $3 < Z < 8$ had little effect on the results. We also require that any matter flux have a velocity $|v_p| > 0.1$, which corresponds to an observationally interesting $v \sim 200$ km/s. We note that non-trivial outflows are gen-

erated for dynamo number $N_d = 10$. The outflows begin at approximately $t = 150$ inner disc orbits, corresponding to a time $t \sim 5$ yrs for T Tauri stars. This is when the dipole moment reaches its saturation value and the plasma $\beta < 1$ in the inner parts of the disc near $R = R_{\text{dyn}}$. Disc dynamos are therefore suitable candidates to explain time varying outflows observed in T Tauri systems with observed time scales between outflows of $10 - 100$ yrs. Such a model has previously been explored by Stepanovs, Fendt and Sheiknezami (2014) where the dynamo was explicitly turned on and off to produce time varying outflows. Though oscillatory, the mass flux $\dot{M} \approx 0.025$ or approximately $6.8 \times 10^{-9} M_\odot/\text{yr}$ for a T Tauri star, which is consistent with observational values. The start of outflow generation corresponds to a decrease in the ratio of matter to magnetic pressure β . We plot this parameter, averaged over the thickness of the disc, as a function of radius for $t = 0, 100, 200$ and 300 in Fig. 10. Winds are primarily launched from the inner part of the disc. We see that the region $R_* < R < 5$ becomes magnetically dominated ($\beta < 1$) for $t > 200$, consistent with the formation of a gap for $R < R_{\text{dyn}}$. The time of outflow generation also corresponds to the time at which the stellar multipoles asymptote to their late time values. At this time our linear analysis (10) breaks down because we can no longer ignore the v_z velocity component. Flux can now flow in the Z direction, thereby halting the growth of flux on the surface of the star. We note that though the stellar dipole and octupole moments saturate, other features of the disc remain non-stationary - the stellar mass flux and mass flux in the wind continue to vary with time. This is consistent with the picture that winds are primarily affected by the disc, in particular near the inner disc where the mass flux is greatest. Outflows can be enhanced via dynamo growth on time scales of the simulation. Cowling's theorem can be circumvented because the timescales for magnetic field growth are shorter than the diffusion timescale.

3.1.4 Dipole Seed Field

The time when significant outflows are generated corresponds to the time when the dipole moment reaches its saturation value of $\mu_{\text{dip}} \approx 3$. We compare this to a run where the initial magnetic field is a dipole with magnetic moment $\mu_{\text{dip}} = 3$, corresponding to this late time magnetic moment of the dynamo generated field. We keep other parameters unchanged, $\alpha_d = \alpha_\eta = \alpha_\nu = 0.1$. This field configuration generates outflows roughly an order of magnitude smaller than the late time dynamo configuration, but at earlier times - since the stellar dipole moment is already present, it can begin generating outflows right away without first having to be generated in the disc. Torkelsson and Brandenburg (1994a) showed that if a stellar dipole is used as the seed field, the field generated in the disc has opposite polarity. Dyda et al. (2015) showed that anti-aligned stellar dipole and disc fields had suppressed outflows compared to a purely disc field because the field line structure in the inner part of the disc was not conducive to mass loading. Our results here are consistent with this, where the case with a seed disc field has the strongest outflows. If the dynamo is turned off, this stellar dipole configuration settles to a configuration with $\mu_{\text{dip}} \approx 2.5$ and the higher order moments

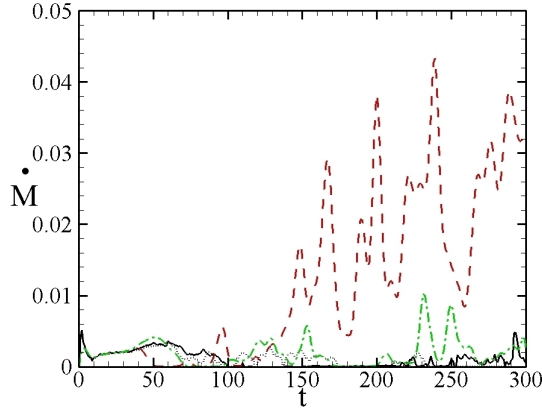


Figure 9. Total mass flux \dot{M} as a function of time for dynamo numbers $N_d = 0$ (black, dotted), 1 (black, solid), 5 (green, dash-dot), 10 (red, dash) ($\alpha_d = 0, 0.01, 0.05, 0.1$). Observationally significant outflows occur after $t = 150$.

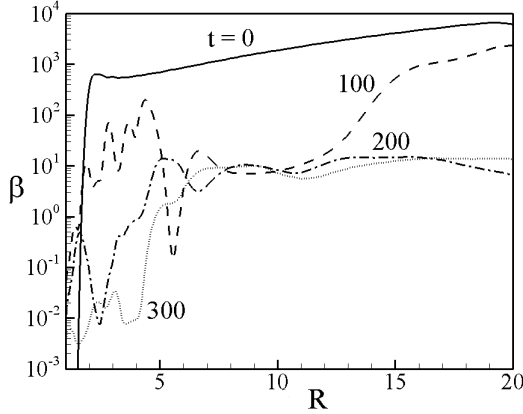


Figure 10. Plasma $\beta = 8\pi P/|B|^2$ as a function of radius for $t = 0$ (solid), 100 (dash), 200 (dash-dot) and 300 (dotted) in the case $\alpha_d = 0.1$. Note that when the inner disc $R < 5$ becomes magnetically dominated, an inner disc wind begins to outflow.

are zero. If the dynamo is turned on, the dipole moment grows and saturates to $\mu_{\text{dip}} \approx 4$, and the octupole moment saturates to $\mu_{\text{oct}} \approx -0.5$. We observe the same behaviour as for the disc field where the dipole and octupole have the same sign until saturation, at which time it quickly reverses direction. Though the disc dynamo generates a dipole component of the magnetic field, it is unclear whether a disc dynamo can generate a closed magnetosphere which has been shown to generate strong outflows in the propeler regime.

3.1.5 Magnetic Diffusivity

We vary the dynamo number by keeping $\alpha_d = 0.1$ fixed and varying the magnetic diffusivity from $0.03 \leq \alpha_\eta \leq 0.3$. The viscosity is also kept constant at $\alpha_\nu = 0.3$. Below we plot the dipole moment as a function of time for these various runs. As before, the dipole moment saturates to a certain

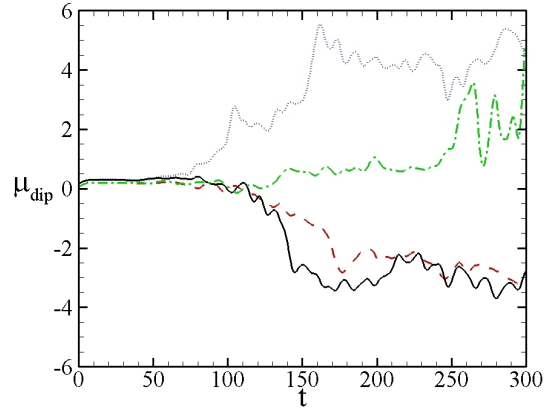


Figure 11. Dipole moment μ_{dip} as a function of time for fixed $\alpha_d = 0.1$ and viscosity $\alpha_\nu = 0.3$ with varying magnetic diffusivity $\alpha_\eta = 0.1$ (black, solid), 0.07 (red, dash), 0.05 (green, dash-dot) and 0.03 (blue, dotted).

value. Interestingly, the sign of the dipole moment depends on the magnetic diffusivity. For $\alpha_\eta \leq 0.05$ then $\mu_{\text{dip}} > 0$ and for $\alpha_\eta \geq 0.07$ then $\mu_{\text{dip}} < 0$ (Fig. 11). Empirically the field line structure is different in these two regimes. In the case of larger diffusivity, the field lines in the outer part of the disc are mostly vertical, threading through the disc. In contrast, for the smaller diffusivity cases the field lines are nearly parallel with the disc. This is what we would expect as field lines will naturally tilt towards the disc if they are frozen in to the matter and the matter accretes inwards. Decreasing the dynamo parameter $\alpha_d = 0.01$ had no effect on the sign of the generated dipole moment - in fact, the late time value $\mu_d \propto \alpha_d^{-1/2}$ holds for $\alpha_d < 0.1$ suggesting that the effect is not due to a changing dynamo number. Rather, the sign of the late time dipole moment depends on the sign of the poloidal field at early times near the star. This is controlled by the relative strengths of viscous and diffusive effects. The sign change in the generated dipole is likely due to an increase in viscous effects in the disc. The Prandtl number in the case where a large positive dipole grew was $\mathcal{P} = 10$ whereas for other runs this ratio was $\mathcal{P} \lesssim 1$. In cases where the late time dipole moment asymptotes to a negative value, the poloidal field in the upper hemisphere is negative at early times. This is reversed for cases where the dipole moment asymptotes to a positive value. As described in Section 2.2, changing the relative strength of the viscosity and diffusivity changes the sign of a term governing the flux function evolution. Since the flux function is coupled to the toroidal field, we expect this to change the sign of the toroidal field.

3.2 Strong Dynamo

For $\alpha_d > 0.1$ the evolution of the disc is qualitatively different. We set $\alpha_\eta = \alpha_\nu = 0.1$ and take $\alpha_d = 0.2, 0.28$ and 0.5 . Below we show poloidal plots of the disc density ρ , magnetic flux contours Ψ and poloidal velocity vectors v_p of a typical run in the strong dynamo regime in Fig. 12 for the representative case of $\alpha_d = 0.28$. Magnetic loops form for all radii $R > R_{\text{dyn}}$ unlike in the weak dynamo regime where

loops only form close to R_{dyn} . Though loops form along the entire length of the disc, the magnetic pressure is strongest in the inner portions of the disc. This innermost loop opens up due to the differential rotation of the disc and pushes out the flux from the outer disc. Because the dynamo is much stronger, the disc becomes magnetically dominated and unstable. The dynamo time scale is too short compared to the viscous and diffusive time scales and disrupts the global evolution of the disc on orbital time scales.

Suppose that to become dynamically significant, the seed field must grow by some factor $f > 1$. Then from (15) we get rapid dipole mode growth in one rotation period if $\alpha_d(3+4\alpha_d) > (f/2\pi)^2$. To become magnetically dominated $f \sim -\frac{1}{2} \ln \beta(0) \sim \frac{1}{2} \ln(10^3) \approx 3.5$ using typical simulation seed field values. This yields $\alpha_d \gtrsim 0.09$, so roughly what was found empirically for the transition from the weak to the strong dynamo regime.

As the field grows and dominates the disc dynamics on orbital time scales the disc warps and breaks up as a gap opens near $R \sim R_{\text{dyn}}$ where the magnetic pressure is greatest. Because the disc becomes unstable and breaks up we can only study these cases for $t \sim 100$ inner disc orbits. The linear theory, (14) suggests that the growth rate $\sigma \propto \alpha_d$ when $\alpha_d \sim 1$. However this is not seen in our simulations. In this regime we do not see a period of exponential growth suggesting that if it occurs, it is for such a short period of time as to be unnoticeable. The gap can open on much faster time scales owing to an accretion rate of order a few larger than in the weak dynamo regime. The loop like structure of the generated field causes the field components to alternate signs in the disc plane, and field anihilations lead to chaotic behaviour.

4 CONCLUSION

We investigated the effects of an α -dynamo operating within an accretion disc. Simulation results were affected by three dimensionless parameters controlling the dynamo strength α_d , the disc viscosity α_ν and the magnetic diffusivity α_η . Our main findings are summarized below.

1. An initial poloidal seed magnetic field threading the disc grows via the disc dynamo - the differential rotation of the disc creates a toroidal magnetic field, which is converted to poloidal magnetic field via dynamo action. This process repeats until at late times the poloidal field strength saturates to a value $\propto \sqrt{\alpha_d}$. The local growth rate of the field during early times is exponential and set by the local Keplerian velocity and the strength of the dynamo with $\sigma \propto \Omega_K \alpha_d^{1/2}$
2. The dynamo excites dipole and octupole modes, allowing for the growth of these modes on the star. Quadrupole modes are suppressed at late times, owing to the symmetry of the initial seed field. Dipole and octupole modes saturate to values of opposite polarity with magnitudes $\propto \sqrt{\alpha_d}$. This has interesting observational consequences since a disc dynamo could be responsible for the observed dipole and higher order multipoles observed on T Tauri stars.
3. A seed field that is too small to generate observationally interesting outflows can grow on time scales $\tau \sim \Omega_K^{-1} \alpha_d^{-1/2}$ to values which are high enough to launch observationally significant outflows. This suggests that disc dynamos may

be important in generating the large scale, ordered magnetic fields needed for MHD launched outflows.

4. A stellar dipole seed field generates a field with outflows ~ 10 weaker than a disc seed field because of interactions between the late time disc field and the stellar dipole. This may be useful in distinguishing between systems that advected their magnetic field from the ISM and those that generated them local via a dynamo mechanism.

5. Increasing the Prandtl number causes the polarity of the late time dipole moment to change. The disc dynamo phase space is more complex than simply α_d as might naively be thought - it is jointly a function of three time scales: the dynamo, viscous and diffusive times.

6. For larger values of the dynamo parameter $\alpha_d \gtrsim 0.1$ the disc becomes magnetically dominated on time scales $\tau \sim \Omega_K^{-1}$ - a gap forms in the inner disc where the dynamo is strongest, eventually leading to the break up of the entire disc as the growth of the field goes unchecked.

Physically these findings can be reconciled by understanding that three time scales are at play - the dynamo time scale, the viscous time scale and the diffusive time scale. If the dynamo time scale dominates, the viscous disc becomes magnetically dominated and breaks up. This is the “strong dynamo” regime and corresponds to the states described in Stepinski & Levy (1988) who concluded that strong local dynamo modes could disrupt the global modes of the disc. If the diffusive time scale dominates then the field does not grow sufficiently to launch outflows. When time scales are comparable we are in the “weak dynamo” regime where outflows can be enhanced but the overall disc dynamics are not disrupted. The relative strength of the viscous and diffusive effects determines the sign of the late time dipole field.

ACKNOWLEDGMENTS

Resources supporting this work were provided by the NASA High-End Computing (HEC) Program through the NASA Advanced Supercomputing (NAS) Division at the NASA Ames Research Center and the NASA Center for Computational Sciences (NCCS) at Goddard Space Flight Center. S.D and R.V.E.L were supported by NASA grant NNX14AP30G and NSF grant AST-1211318. A.V.K acknowledges the support from the Russian Academic Excellence Projects “5top100”. I.W acknowledges support from NASA grant NNX13AH42G.

APPENDIX A: NUMERICALLY EXTRACTING MULTIPOLE MOMENTS

Any magnetic field can be described by its multipole expansion. Below, we derive formulae for the axisymmetric dipole, quadrupole and octupole components of a magnetic multipole expansion in terms of surface integrals in cylindrical coordinates. These are used to numerically extract the multipole coefficients of the magnetic field configurations in our simulations.

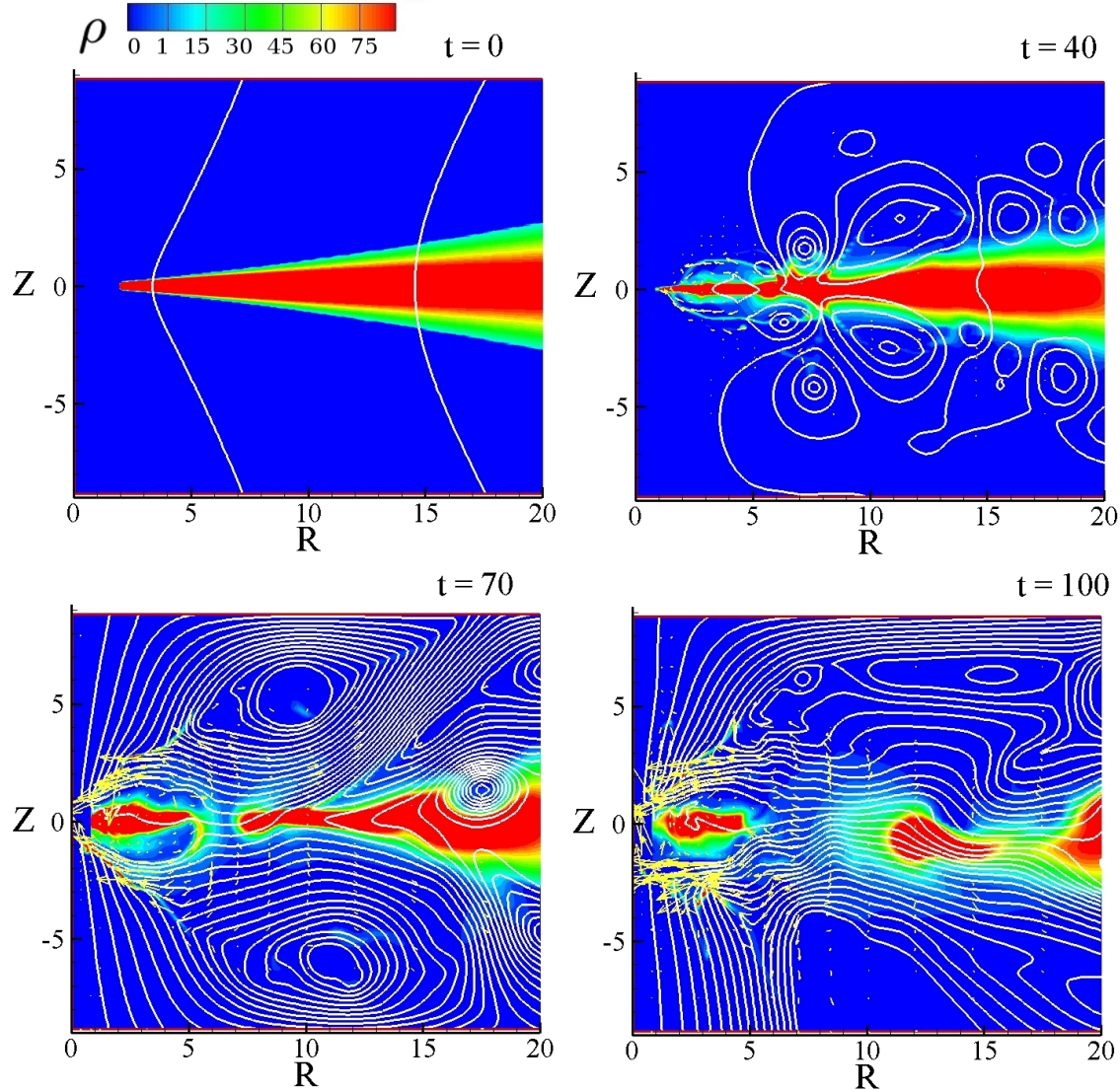


Figure 12. Density ρ (color), poloidal field lines Ψ (white) and poloidal velocity v_p for the case $N_d = 28$ ($\alpha_d = 0.28$). $t = 0$ shows the initial large scale seed field. By $t = 40$ magnetic loops have formed along the entire length of the disc. At $t = 70$ we can see the quadrupolar nature of the field as loops are advected inwards. At late times these loops expand into open field lines. The magnetic pressure has grown enough to seriously disrupt the disc and open a gap at $R_{\text{dyn}} = 5$.

A1 Dipole Moment

Consider a dipole moment, symmetric about the Z -axis with flux function given by

$$\Psi = \mu_{\text{dip}} \frac{R^2}{(R^2 + Z^2)^{3/2}}, \quad (\text{A1})$$

and poloidal magnetic fields

$$B_R = 3\mu_{\text{dip}} \frac{RZ}{(R^2 + Z^2)^{5/2}}, \quad (\text{A2})$$

$$B_Z = \mu_{\text{dip}} \frac{(2Z^2 - R^2)}{(R^2 + Z^2)^{5/2}}. \quad (\text{A3})$$

Given a general magnetic field, we want to extract its dipole moment from its multipole expansion at any given time. In

general the dipole moment is given by

$$\mathbf{m} = \frac{1}{2} \int d\mathbf{V} [\mathbf{r} \times \mathbf{J}] = \frac{c}{8\pi} \int d\mathbf{V} [\mathbf{r} \times (\nabla \times \mathbf{B})], \quad (\text{A4})$$

where we work in CGS units and have used Ampere's law. We will integrate over a cylinder $0 < R < a$, $-h < Z < h$, $0 < \phi < 2\pi$ enclosing the star. We also assume the boundary condition $\Psi(0, Z) = 0$. Using vector identities we may write

$$\mathbf{m} = \frac{c}{8\pi} \int d\mathbf{V} [\nabla(\mathbf{r} \cdot \mathbf{B}) - (\mathbf{r} \cdot \nabla)\mathbf{B} - (\mathbf{B} \cdot \nabla)\mathbf{r}]. \quad (\text{A5})$$

We are interested in the \hat{Z} component of the magnetic moment, μ_{dip} . We calculate the contribution to μ_{dip} from each

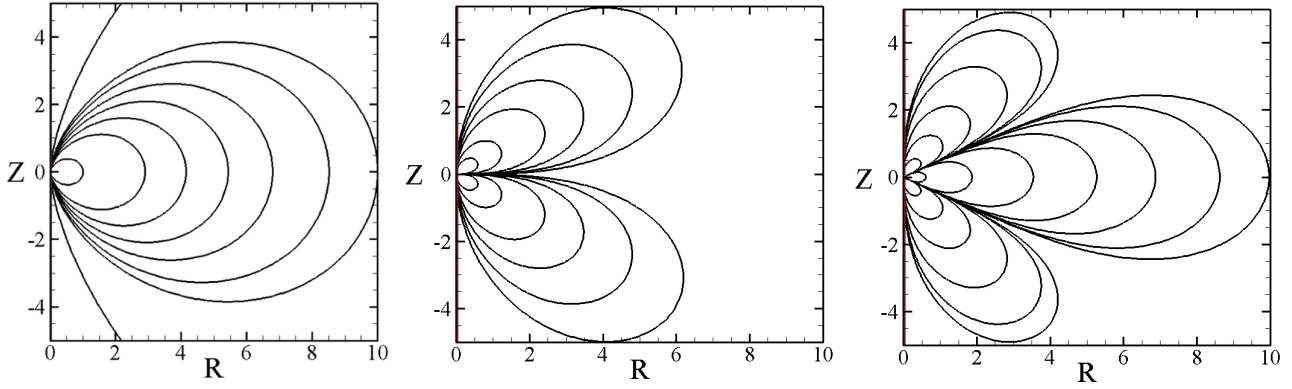


Figure A1. Flux lines of axially symmetric dipole (left), quadrupole (center) and octupole (right).

of the above three terms below.

$$\begin{aligned} T_1 &\equiv \int d\mathbf{V} \nabla_Z (\mathbf{r} \cdot \mathbf{B}) = \int d\mathbf{S}_Z (\mathbf{r} \cdot \mathbf{B}) \\ &= 2\pi \int_0^a R dR (\mathbf{r} \cdot \mathbf{B}) \Big|_{-h}^h, \end{aligned} \quad (\text{A6})$$

where we have used the divergence theorem to convert the volume integral to a surface integral over the sides of the cylinder and only the top and bottom contribute to the Z-component. Using the definition of magnetic field in terms of the flux function we may write

$$T_1 = 2\pi \int_0^a dR R^2 B_R \Big|_{-h}^h + 2\pi h [\Psi(a, h) + \Psi(a, -h)]. \quad (\text{A7})$$

The Z-component contribution from the second term is

$$\begin{aligned} T_2 &= - \int d\mathbf{V} [(\mathbf{r} \cdot \nabla) \mathbf{B}]_Z \\ &= -2\pi \int R dR dZ \left(R \frac{\partial}{\partial R} + Z \frac{\partial}{\partial Z} \right) B_Z. \end{aligned} \quad (\text{A8})$$

Integrating the first term by parts and using the definition of the magnetic flux function we may write

$$T_2 = -2\pi \int_{-h}^h dZ \left[a^2 B_Z(a, Z) - 2\Psi(a, Z) - R Z B_R(a, Z) \right]. \quad (\text{A9})$$

The third term can be dealt with by rewriting it in terms of the flux function and explicitly carrying out the integration in R to yield

$$T_3 = -2\pi \int_{-h}^h dZ \Psi(a, Z). \quad (\text{A10})$$

Combining these terms we arrive at the result

$$\begin{aligned} \mu_{\text{dip}} &= \frac{c}{4} \left\{ \int_0^a dR R^2 B_R(R, Z) \Big|_{-h}^h + h [\Psi(a, h) + \Psi(a, -h)] \right. \\ &\quad \left. - \int_{-h}^h dZ \left[a^2 B_Z(a, Z) - \Psi(a, Z) - a Z B_R(a, Z) \right] \right\}, \end{aligned} \quad (\text{A11})$$

which is easy to implement in our cylindrical code.

A2 Quadrupole Moment Calculation

Consider a quadrupole moment, symmetric about the Z-axis with flux function given by

$$\Psi = \frac{3\mu_{\text{quad}}}{4} \frac{R^2 Z}{(R^2 + Z^2)^{5/2}}, \quad (\text{A12})$$

and poloidal magnetic fields

$$B_R = -\frac{3\mu_{\text{quad}}}{4} \frac{R(R^2 - 4Z^2)}{(R^2 + Z^2)^{7/2}}, \quad (\text{A13})$$

$$B_Z = \frac{3\mu_{\text{quad}}}{4} \frac{(Z^2 - 3R^2)}{(R^2 + Z^2)^{7/2}}. \quad (\text{A14})$$

Its quadrupole moments are $D_{11} = D_{22} = -D_{33}/2$ where

$$\begin{aligned} \mu_{\text{quad}} \equiv D_{33} &= \int d\mathbf{V} [\mathbf{r} \cdot (\nabla \times \mathbf{J})] Z^2 \\ &= 2 \int d\mathbf{V} Z (\mathbf{r} \times \mathbf{J})_Z \end{aligned} \quad (\text{A15})$$

where as with the dipole, we are interested in the Z-component of μ_{quad} . Using Maxwell's equations we can write

$$\mu_{\text{quad}} = \frac{c}{2\pi} \int d\mathbf{V} Z [\mathbf{r} \times (\nabla \times \mathbf{B})]_Z. \quad (\text{A16})$$

As with the dipole case, this expression can be expanded using a vector identity as

$$\mu_{\text{quad}} = \frac{c}{2\pi} \int d\mathbf{V} Z \left[\nabla (\mathbf{r} \cdot \mathbf{B}) - (\mathbf{r} \cdot \nabla) \mathbf{B} - (\mathbf{B} \cdot \nabla) \mathbf{r} \right]_Z. \quad (\text{A17})$$

As in the dipole case we calculate each of these terms separately. We are interested in the \hat{Z} component of the quadrupole moment.

$$\begin{aligned} T_1 &\equiv \int d\mathbf{V} Z \nabla_Z (\mathbf{r} \cdot \mathbf{B}) \\ &= - \int d\mathbf{V} (\mathbf{r} \cdot \mathbf{B}) \hat{Z} + Z (\mathbf{r} \cdot \mathbf{B}) \Big|_{-h}^h, \end{aligned} \quad (\text{A18})$$

where we have integrated by parts. Writing out the magnetic field in term of the flux function, we expand the first term and carry out some of the integrals. The second term

we evaluate on the top and bottom of the cylinder which yields

$$T_1 = 2\pi \int_0^a dR R \Psi(R, Z) \Big|_h^h - 2\pi \int_{-h}^h dZ Z \Psi(a, Z) \\ + 2\pi \int_0^a dR R Z (RB_R + ZB_Z) \Big|_{-h}^h. \quad (\text{A19})$$

Expanding the second term and carrying out the angular integral we find

$$T_2 \equiv - \int d\mathbf{V} Z (\mathbf{r} \cdot \nabla) \mathbf{B} \\ = - 2\pi \int dR dZ \left(Z R^2 \frac{\partial B_z}{\partial R} + Z^2 R \frac{\partial B_z}{\partial Z} \right). \quad (\text{A20})$$

Performing integration by parts for the R integral on the first term and then writing it out in terms of the flux function allows the integral in R to be evaluated, yielding

$$T_2 = 2\pi \int_{-h}^h dZ 2Z \Psi(a, Z) - a^2 Z B_z(a, Z) \\ + 2\pi \int_{-h}^h dZ a Z^2 B_R(a, Z). \quad (\text{A21})$$

For the final term, we take the divergence, expand it in terms of the flux function, carry out the integral in R and find

$$T_3 = - \int d\mathbf{V} Z (\mathbf{B} \cdot \nabla) Z = - 2\pi \int_{-h}^h dZ Z \Psi(a, Z). \quad (\text{A22})$$

Combining these terms we arrive at the result

$$\mu_{\text{quad}} = c \int_0^a dR \left[R \Psi(R, Z) + R Z (RB_R + ZB_Z) \right] \Big|_{-h}^h \\ + c \int_{-h}^h dZ \left[a Z^2 B_R(a, Z) - a^2 Z B_z(a, Z) \right]. \quad (\text{A23})$$

A3 Octupole Moment Calculation

Consider an octupole moment, symmetric about the Z-axis with flux function given by

$$\Psi = \frac{\mu_{\text{oct}}}{2} \frac{R^2 (4Z^2 - R^2)}{(R^2 + Z^2)^{7/2}}, \quad (\text{A24})$$

and poloidal magnetic fields

$$B_R = \frac{5\mu_{\text{oct}}}{2} \frac{R Z (4Z^2 - 3R^2)}{(R^2 + Z^2)^{9/2}}, \quad (\text{A25})$$

$$B_Z = \frac{\mu_{\text{oct}}}{2} \frac{(8Z^4 - 24Z^2 R^2 + 3R^4)}{(R^2 + Z^2)^{9/2}}. \quad (\text{A26})$$

The octupole moment is given by

$$\mu_{\text{oct}} \equiv 2\sqrt{\frac{\pi}{7}} M_{30}, \quad (\text{A27})$$

where

$$M_{30} = \frac{1}{4} \int d\mathbf{V} [\mathbf{r} \times \mathbf{J}] \cdot \nabla (r^3 Y_{30}), \quad (\text{A28})$$

and

$$r^3 Y_{30} = \sqrt{\frac{7}{4\pi}} r^3 P_3(\cos \theta) = \frac{1}{4} \sqrt{\frac{7}{\pi}} Z (2Z^2 - 3R^2), \quad (\text{A29})$$

is a spherical harmonic that we have written in terms of the Legendre polynomial P_3 . Expanding the cross product and using Ampere's law to write out the current in terms of the magnetic field and evaluating the azimuthal integral we find

$$\mu_{\text{oct}} = \frac{3c}{16} \left[4 \int dR dZ R^2 Z^2 \left(\frac{\partial B_R}{\partial Z} - \frac{\partial B_Z}{\partial R} \right) \right. \\ \left. - \int dR dZ R^4 \left(\frac{\partial B_R}{\partial Z} - \frac{\partial B_Z}{\partial R} \right) \right]. \quad (\text{A30})$$

Evaluate each of these terms separately. The first term is

$$T_1 \equiv \int dR dZ R^2 Z^2 \left(\frac{\partial B_R}{\partial Z} - \frac{\partial B_Z}{\partial R} \right) \\ = \int dR R^2 h^2 B_R \Big|_{-h}^h - 2 \int dR dZ R \Psi + 2 \int dR R Z \Psi \Big|_{-h}^h \\ - \int dZ Z^2 a^2 B_Z(a, Z) + 2 \int dZ Z^2 \Psi(a, Z), \quad (\text{A31})$$

where we have used integration by parts and the definition of magnetic field in terms of the magnetic flux function. Similarly, the second term is

$$T_2 \equiv \int dR dZ R^4 \left(\frac{\partial B_R}{\partial Z} + \frac{\partial B_Z}{\partial R} \right) \\ = \int dR R^4 B_R \Big|_{-h}^h - \int dZ a^4 B_Z(a, Z) \\ - 8 \int dR dZ R \Psi + 4 \int dZ a^2 \Psi(a, Z). \quad (\text{A32})$$

Combining these terms we find

$$\mu_{\text{oct}} = \frac{3c}{16} \left[4 \int dR R^2 h^2 B_R \Big|_{-h}^h + 8 \int dR R Z \Psi \Big|_{-h}^h \right. \\ - 4 \int dZ Z^2 a^2 B_Z(a, Z) + 8 \int dZ Z^2 \Psi(a, Z) \\ - \int dR R^4 B_R \Big|_{-h}^h + \int dZ a^4 B_Z(a, Z) \\ \left. - 4 \int dZ a^2 \Psi(a, Z) \right]. \quad (\text{A33})$$

We note the cancellation of the volume integrals in T_1 and T_2 , allowing the final expression to again only depend on surface integrals.

REFERENCES

- Bai, X.N., Stone, J.M., 2013, ApJ, 763, 30.
- Bardou, A., von Rekowski, B., Dobler, W., Brandenburg, A., Shukurov, A., 2001, A&A, 370, 635–648.
- Brandenburg, A., Nordlund, A., Stein, R.F. & Torkelsson, U., 1995, ApJ, 446, 741.
- Cowling, T.G., 1934, MNRAS 94:39.
- Davis, S.W., Stone, J.M., Pessah, M.E., 2010, ApJ, 713, 52.

Del Zanna, L., Bugli, M., Bucciantini, N., 2014, arXiv:1401.3223v1

Donati, J-F., Collier Cameron, A., 1997, MNRAS, 291,1.

Donati, J-F., Collier Cameron, A., Hussain, G.A.J., Semel, M., 1999, MNRAS, 302,437.

Donati, J.F., Gregory, S.G., Alencar, S.H.P., Hussain, G., Bouvier, Dougados, C., Jardine, M.M., Menard, F., Romanova, M.M., MaPP collaboration, 2012, MNRAS, 425:2948-2963.

Donati, J.F., Gregory, S.G., Alencar, S.H.P., Hussain, G., Bouvier, J., Jardine, M.M., Menard, F., Dougados, C., Romanova, M.M., MaPP collaboration, 2013, MNRAS, 436:881-897.

Dyda, S., Lovelace, R.V.E., Ustyugova, G.V., Lii, P.S., Romanova, M.M., Koldoba, A.V., 2015, MNRAS, 450:481-493.

Guan, X., & Gammie, C.F. 2009, ApJ, 697, 1901

Jardine, M., Wood, K., Collier Cameron, A., Donati, J-F., Mackay, D.H., 2002, MNRAS, 336, 1364.

Koldoba, A., Ustyugova, G., Romanova, M.M., Lii, P., Comins, C., Dyda, S., Lovelace, R.V.E., 2015, New Astronomy, submitted.

Kulsrud, R.M., Annu. Rev. Astron. Astrophys, 1999, 37:37-64.

Kulsrud, R.M., Plasma Physics for Astrophysics, 2005.

Lii, P., Romanova, M.M., & Lovelace, R.V.E. 2012, MNRAS, 420, 2020

Romanova, M.M, Ustyugova, G.V., Koldoba, A.V., Chechetkin, V.M., Lovelace, R.V.E. 2002, ApJ, 578, 420

Sadowski, A., Narayan, R., Tchekhovskoy, A., Abarca, D., Zhu, Y., McKinney, J.C., 2014, arXiv:1407.4421v1

Schober, J., Schleicher, D., Federrath, C., Glover, S., Klessen, R.S., Banerjee, R., 2012, ApJ, 754:99-107.

Shi, J., Krolik, J.H., Hirose, S., 2010, ApJ, 708, 1716.

Simon, J.B., Beckwith, K., Armitage, P.J., 2012, MNRAS, 422, 2685.

Shakura, N.I., & Sunyaev, R.A. 1973, A&A, 24, 337

Shu, F.H., Adams, F.C., Lizano, S., 1987, Ann. Rev. Astron. 25:23.

Stepinski, T.F., Levy, E.H., 1988, ApJ, 331:416-434.

Stepanovs, D., Fendt, C., Sheiknezami, S., 2014, ApJ, 796:29.

Stone, J.M., Hawley, J.F., Gammie, C., Balbus, S.A., ApJ, 463:656-673.

Torkelsson, U., Brandenburg, A., 1994a, A&A, 283:677.

Torkelsson, U., Brandenburg, A., 1994b, Chaos, Solitons & Fractals, 5(10):1975-1984.

Torkelsson, U., Brandenburg, A., 1994c, A&A, 292:341-349.

Tout, C.A., Pringle, J.E., 1992, MNRAS, 259:604-612.

Vidotto, A.A., Gregory, S.G., Jardine, M., Donati, J.F., Petit, P., Morin, J., Folsom, C.P., Bouvier, J., Cameron, A.C., Hussain, G., Marsden, S., Waite, I.A., Fares, R., Jeffers, S., do Nascimento, J.D., 2014, MNRAS, 441:2361-2374.

von Rekowski, B., Brandenburg, A., Dobler, W. & Shukurov, A. 2003, A&A, 398, 825

Zanni, C., Ferrari, A., Rosner, R., Bodo, G., Massaglia, S., 2007, A&A 469, 811828